8-2020

Development of microfluidic bubble perfusion device for neuropeptide analysis from ex vivo brain slice models

Victoria Norman
vnorman1@utk.edu

To the Graduate Council:

I am submitting herewith a thesis written by Victoria Norman entitled "Development of microfluidic bubble perfusion device for neuropeptide analysis from ex vivo brain slice models." I have examined the final electronic copy of this thesis for form and content and recommend that it be accepted in partial fulfillment of the requirements for the degree of Master of Science, with a major in Chemistry.

, Major Professor

We have read this thesis and recommend its acceptance:

Accepted for the Council:
Dixie L. Thompson

Vice Provost and Dean of the Graduate School

(Original signatures are on file with official student records.)

Development of microfluidic bubble perfusion device for neuropeptide analysis from *ex vivo* brain slice models

A Thesis Presented for the
Master of Science
Degree
The University of Tennessee, Knoxville

Victoria Nickole Norman
August 2020

DEDICATION

This work is dedicated to my parents, James and Kathy, who are always just a phone call away. Thank you for the unconditional love, support, and for being a source of motivation and strength.

ABSTRACT

Characterized by social impairments, repetitive or compulsive behaviors, and speech deficits, the underlying causes of Autism Spectrum Disorder (ASD) are currently unknown. Both oxytocin and arginine vasopressin are involved in regulating social behaviors in mammals and the dysregulation of each is thought to play a role in social impairments associated with ASD. Studying the secretion dynamics of these peptides can help us better understand regulatory relationships that may be involved in neurodevelopmental disorders like ASD. Microfluidic brain slice culture is an important tool for *ex vivo* modeling of basal and diseased state neurochemistry. A significant challenge to culturing brain slices in microfluidic flow systems is the efficient delivery of oxygen to enable medium to long-term viability of tissue slice. A microfluidic slice culture device that delivers continuous flow of carbogen gas-segmented culture media droplets to an immobilized brain tissue slice for total perfusion, enabling efficient oxygenation has been developed. The size of tissue slices, and the dimensions of the required tissue chamber present a lower limit of droplet volume on the order of 10 µL, which is a relatively large volume compared to many microfluidic systems. For downstream assay of cellular secretions, sample preconcentration is needed. An electrophoretic platform for sample preconcentration within the gas-segmented perfusate droplets has been developed.

TABLE OF CONTENTS

LIST OF FIGURES

CHAPTER 1. INTRODUCTION

1.1 Autism Spectrum Disorder

Autism Spectrum Disorder (ASD) is a developmental disorder characterized by abnormal social interaction, repetitive or compulsive behaviors, speech deficits, and restricted interest.[1,2] Presentation of autistic features varies and can range from mild to severe.[3] Individuals also show varying cognitive development, ranging from those who function well above average to those who show intellectual disabilities.[3] The Centers for Disease Control and Prevention has been tracking the prevalence of ASD since 1996 through the Autism and Developmental Disabilities Monitoring (ADDM) Network. In 2016, the combined ASD prevalence, with data from all ADDM sites, was one in 54 children aged 8 years.[4] While ASD is a disorder with strong genetic correlations, no single genetic mutation accounts for more than 1-2% of ASD cases.[2,5] Assessment of chromosomal variations, as well as other gene related studies have shown a wide range in genes with predisposing mutations and polymorphisms associated with ASD.[2] Neuroanatomical studies, one of the various approaches used to study the underlying mechanisms of ASD, have reported abnormal neuronal connectivity in autistic individuals.[2] While the scientific community struggles to identify the key neurophysiological mechanisms of ASD, the neuroendocrine mechanisms involved are relatively less studied.

1.1.1 Neuropeptides of ASD

Oxytocin and arginine vasopressin. Oxytocin (OT) is a hormone that is synthesized by the magnocellular neurons of the supraoptic (SON) and paraventricular (PVN) nuclei within the hypothalamus.[6,7] OT helps induce the production of milk and facilitate uterine contractions during childbirth.[7] Arginine vasopressin (AVP) is a peptide, also synthesized in both the SON and PVN, that regulates the tonicity of body fluids by increasing the amount of solute-free water reabsorbed by the kidneys, which is then returned to the vascular system.[8] In addition to being produced in the same nuclei of the hypothalamus, OT and AVP are also similar in structure. Both neuropeptide structures consist of a six amino acid ring with a three amino acid tail, and only differ by two amino acids, in the third and eighth positions (Figure 1-1).[9–11] These neuropeptides are released into the bloodstream from axon terminals in the posterior pituitary.[12]

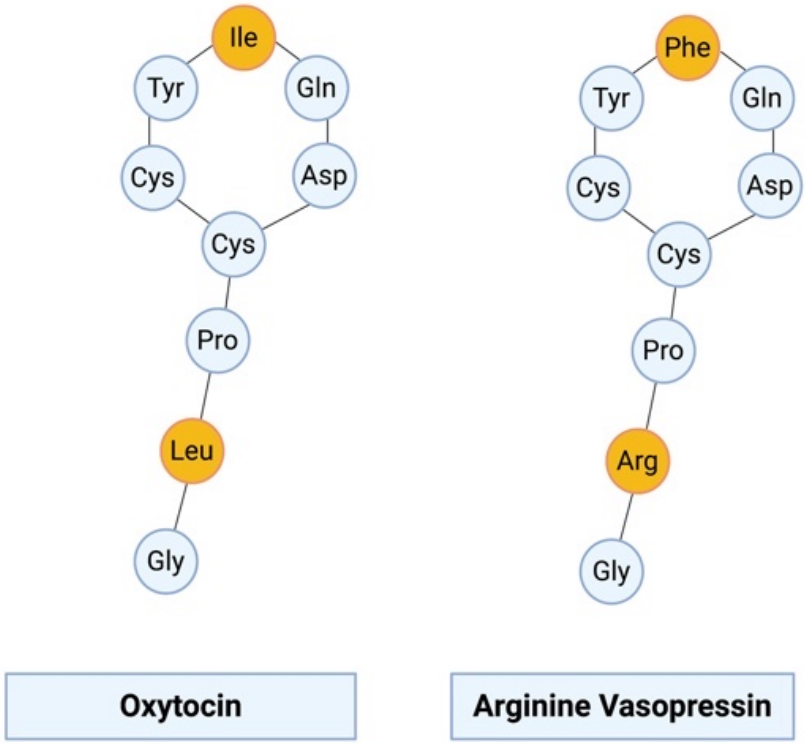

Figure 1-1. *Neuropeptides of ASD.* Diagram of oxytocin and arginine vasopressin, showing the differing amino acids at the third and eighth positions. Full chemical structures of these peptides are given in Figures A-1 and A-2 of the appendix.

There has been high interest in the neuropeptides OT and AVP in ASD because of their role in social and affiliative behavior in animals.[13,14] Extensive research has been conducted and animal studies have shown that both OT and AVP influenced deficits in social and communicative behaviors. For example, Winslow *et al*. demonstrated how the administration of OT and AVP in infant mice reduced distress calls.[14] OT has been shown to reduce natural avoidance of proximity and inhibit defensive behavior and AVP has been linked to social behaviors such as aggression, scent marking and courtship.[11,15] Though studies have shown the implications of OT and AVP in ASD, there is a critical need to better elucidate the neuroendocrine mechanisms of ASD.

Dynorphins. Dynorphins are a class of opioid peptides produced and secreted by magnocellular oxytocin and vasopressin neurons.[16] This class of opioid peptides includes dynorphin A, dynorphin B, and α/β-neo-endorphin, and arises from the precursor protein prodynorphin when it is cleaved by proprotein convertase 2 (PC2).[17] Dynorphins are found widely distributed throughout the central nervous system, but have the highest concentrations in the hypothalamus, medulla, pons, midbrain, and spinal cord.[18] They work at kappa opioid receptors and have been linked to anxiety like behavior and negative emotional states.[19,20] They are also present in the same magnocellular nuclei responsible for synthesis of OT an AVP and have been shown to inhibit OT and AVP secretion.[21,22] While most knowledge in regards to the ability of OT and AVP to regulate social interactions is based on data from animal models, preliminary studies suggests that similar social and stress related effects are present in humans.[7,23] The importance of OT and AVP in stress and in social interactions has been established, suggesting that dysregulation of both may be associated with disorders and psychosocial relevance like ASD. To better understand the regulatory relationships of OT, AVP, and dynorphin new analytical tools are needed for modeling secretion and measuring biologically relevant concentrations in *ex vivo* models.

1.2 Microfluidics for Brain Slice Culturing

The culturing of organotypic brain slices can preserve brain structure and maintain the functionality of neurons within the sliced region while allowing control of the extracellular environment.[24,25] These *ex vivo* models are established tools to study basal and diseases state neurochemistry.[26] Conventional chambers used to culture organotypic brain slices, include interface chambers, which supply a high concentration of oxygen directly to the slice from above, and submerged chambers, where slices are surrounded completely by hyper oxygenated artificial cerebrospinal fluid (aCSF). However, these chambers do not maintain effective nutrient/waste turnover or uniform oxygen exchange.[25,27] Viability of the brain slice is dependent on the diffusion of oxygen into the slice which is limited by the thickness of the tissue.[25] The flow of oxygen and nutrients around the slice is optimal for delivery but is limited by a thickness of approximately 400 μm.[25] Microfluidic devices have shown the potential for

enhanced brain slice viability by improving oxygen and nutrient penetration into slices.[25] Hill *et al.* demonstrates how the efficiency of the nutrient and oxygen exchange is improved by actively flowing aCSF around the tissue.[27] This causes aCSF to be "pushed" or "pulled" through the slice, increasing oxygen availability, thereby improving viability.[27]

1.3 Electrophoresis

Electrophoresis is the movement of charged molecules through a conductive aqueous medium under the influence of an electric field generated by electrodes.[28] Sample is introduced at the anode and flows toward the cathode, while molecules within the sample have different migration times depending on the size of ions and magnitude of charge. Cations migrate towards the negatively charged electrode while anions migrate towards the positively charged electrode with the rate of ion migration depending on the charge-to-size ratio. Ions with higher charge will migrate faster than ions with a lower charge that are the same size and smaller ions will migrate faster than larger ions with the same charge. Neutral molecules are not affected by the electric field.

The bulk flow of buffer solution under the influence of the electric field is known as electroosmotic flow (EOF).[28] The phenomenon is due to the formation of an electric double layer on the inner surface of the separation channel. For example, in capillary electrophoresis, the wall of the capillary has an excess charge due to ionization or the adsorption of ionic species at the surface. A capillary wall coated with fused silica has a surface made of silanol groups. The silanol groups are ionized to negatively charged silanolate groups that will attract cations from the run buffer and form an inner layer of cations at the wall of the capillary, known as the fixed layer.[28] All the negative charges on the capillary surface are fully neutralized by the formation of a mobile layer of cations, that is not tightly held because it is further away from the silanolate groups. Due to the presence of both the fixed and mobile layers, a diffuse double layer of cations forms. The cations present in the diffuse layer carry the bulk of the buffer solution with them in the presence of an electric field, leading to the formation of EOF.

The electrical imbalance that is generated between the fixed and mobile layers is known as the zeta potential (ξ).[29] The EOF is proportional to the zeta potential and the velocity of the EOF is given by (Eq. 1):

$$V_{EOF} = \frac{\varepsilon \zeta E}{4\pi\eta} \qquad (1)$$

where *E* is the applied electric field, ε is the dielectric constant, and η is the viscosity of the buffer.[29] Unlike the velocity of the EOF, the electroosmotic mobility is independent of the applied electric field and only depends on the characteristics of the buffer.[28] The electroosmotic mobility is given by (Eq. 2):

$$\mu_{EOF} = \frac{\varepsilon\zeta}{4\pi\eta} \quad (2)$$

1.4 COMSOL Multiphysics

COMSOL Multiphysics is a cross-platform finite element analysis (FEA) solver and Multiphysics simulation software. FEA is a numerical method used to solve problems of engineering and mathematical models, expressed as partial differential equations, using an array of mathematical techniques.[30] It allows a representative model of a real-life object to be developed and that model can be used to make observations about what that object would do when met with a specific boundary condition. A problem is split into smaller, simpler parts; a finite number of elements. Equations that model these finite elements are solved and assembled back into the larger system of equations that model the entire problem.[31]

FEA is governed by the principle of minimization of energy.[30] When certain boundary conditions are applied to a model there are several configurations but only one configuration is realistically possible. Due to the principle of minimization of energy, the only configuration realistically possible is one where the total energy is minimum.

Designed for real-world applications, the COMSOL Multiphysics simulation environment is used to mimic effects that can be observed in the real world. In order to set up and run a simulation, users follow a general modeling workflow regardless of the physics being used or problem being solved. This workflow consists of seven steps: setting up the model environment, building the geometry, specifying material properties, defining physics boundary conditions, creating the mesh, running the simulation, and postprocessing the results.

When first opening the COMSOL application on the desktop, the software will prompt the user to set up the model environment by choosing between the model wizard or a blank model. The model wizard is a guided approach recommended for all users, regardless of experience and background. Next the user is prompted to select the dimensional space of the model as well as the physics interfaces that will used. A wide variety of physics interfaces such as acoustics, electrochemistry, heat transfer, fluid flow, and more are available to simulate. Commonly known Multiphysics, such as joule heating, are automatically pre-coupled with all the appropriate physics when selected but multiple physics can be coupled as needed by the user manually. To complete the setup of the model environment, the user is prompted to select the type of study to apply to the model. The selected study will determine the solvers used to compute the model.

Users can choose from the general studies to determine whether the model will be time dependent or stationary or preset studies for the previous selected physics interfaces can be used.

The next step of the workflow is building the geometry. There are many drawing tools and operations built into the COMSOL software that can be used to create needed geometries. It is also possible to import geometries from external files or sync geometries from design software like AutoCAD through the purchase of add-on products. Once the model geometry is built the materials of the model and their properties can be specified. There are several built in materials provided by the software that can be selected. It is possible to design a model made of various materials by adding specified materials to separate components that compose the model. Depending on the materials and physics selected there may be material properties that need to be defined by the user in order to compute the problem. Material properties tied to physics are indicated by the software.

Once the geometry is built and the material proprieties have been specified, the next step is to define the physics. Mathematical equations can be assigned to the model or parts of the model in order to simulate the physics. This is done by selecting different parts of the geometry and the specifying appropriate equations and physical conditions that describe that part. The equations representative of any of the physical conditions used within COMSOL Multiphysics can be seen by the user and boundary conditions and constraints can be added and changed from the default values as needed.

When all of the boundary conditions and constraints have been defined for the model, the next step is to create a mesh. Users have the choice between a custom mesh, where physics of the model can be removed and not taken into account when the mesh is generated, or the automatically generated mesh, which is adapted to the physics settings within the model. User can choose from shapes, such as triangles, quadrilaterals, tetrahedrons, hexahedrons, pyramids and prisms when manually generating a mesh. Size choices also range from extremely fine to extremely course, making a mesh completely customizable.

The next step in the workflow is to run the simulation. The software will automatically generate plots based on the physics selected in the model. The full Multiphysics problem being computed can be reviewed and edited by the user in the study before the model is computed. Once the model is computed the results can be postprocessed. Immediately after solving, a default plot appears. Existing plots can be modified, or new ones can be created. For example, a plot showing temperature could be easily changed to display voltage or a completely arbitrary expression could be used so the sine of temperature multiplied by three could be shown.

CHAPTER 2. MICROFLUIDIC BUBBLE PERFUSION DEVICE

2.1 Introduction

Microfluidic devices have been shown to improve the efficiency of brain slice culturing by improving oxygen and nutrient delivery to tissues. However, the continuous flow of aCSF used in these types of devices does not allow for time-resolved measurements of tissue secretions that contain biological molecules of interest due to the diffusional mixing of analytes between the time of secretion and collection of the perfusate samples. Correlating neuropeptide secretion changes in the brain with behavior requires high temporal resolution on the seconds timescale. The generation of monodispersed aCSF droplets ensures that the brain slice spends equal amounts of time in media and oxygen thereby improving the exchange. Individual droplets also allow for time resolved sampling by providing information about the brain tissue through the molecules secreted and collected within a droplet during a certain point in time. By keeping the droplets separated, even when they are analyzed downstream, a high-resolution secretion profile is obtained.

Our lab has begun the development of a microfluidic perfusion device designed to enable time-resolved measurements of secreted factors while maintaining high efficiency tissue oxygenation. My colleague, Amirus Saleheen, has developed the microfluidic perfusion device, seen in Figure 2-1, that provides continuous droplets of aCSF segmented with carbogen gas to a chamber containing the brain tissue slice. As droplets enter the chamber and pass over the tissue slice, biological molecules are secreted and carried away with the droplet to be collected and analyzed further downstream. Droplets of aCSF are segmented with carbogen gas by the use of a microfluidic T-junction. In what is known as the squeezing regime, an emerging bubble fills most of the channel and a carrier liquid pushes the dispersed phase forward until it cuts off. Garstecki *et al*. investigated the formation of segmented droplets via the squeezing regime and showed the size of droplets or bubbles is determined by the ratio of the volumetric flow rates of the two immiscible fluids (Eq. 3):

$$\frac{L_d}{W} = \propto_1 + \propto_2 \frac{Q_{disp}}{Q_{cont}} \qquad (3)$$

where L_d is the length of the dispersed segments, *W* is the width of the side channel, Q_{disp} and Q_{cont} are the volumetric flow rates of the dispersed and continuous phase, respectively, and are constants that depend on the geometry of the T-junction.[32] The monodispersed droplets and bubbles produced ensures the brain tissue slice spends an equal amount of time exposed to aCSF and carbogen gas, maximizing oxygen and nutrient exchange, while also allowing for time resolved measurements of perfusate droplets containing cellular secretions.

To prevent the carryover between droplets that was periodically observed when part of a droplet broke off and was left behind in the chamber, droplet volumes need to be greater than 50% of the chamber volume and surfaces within the chamber need to be hydrophilic.

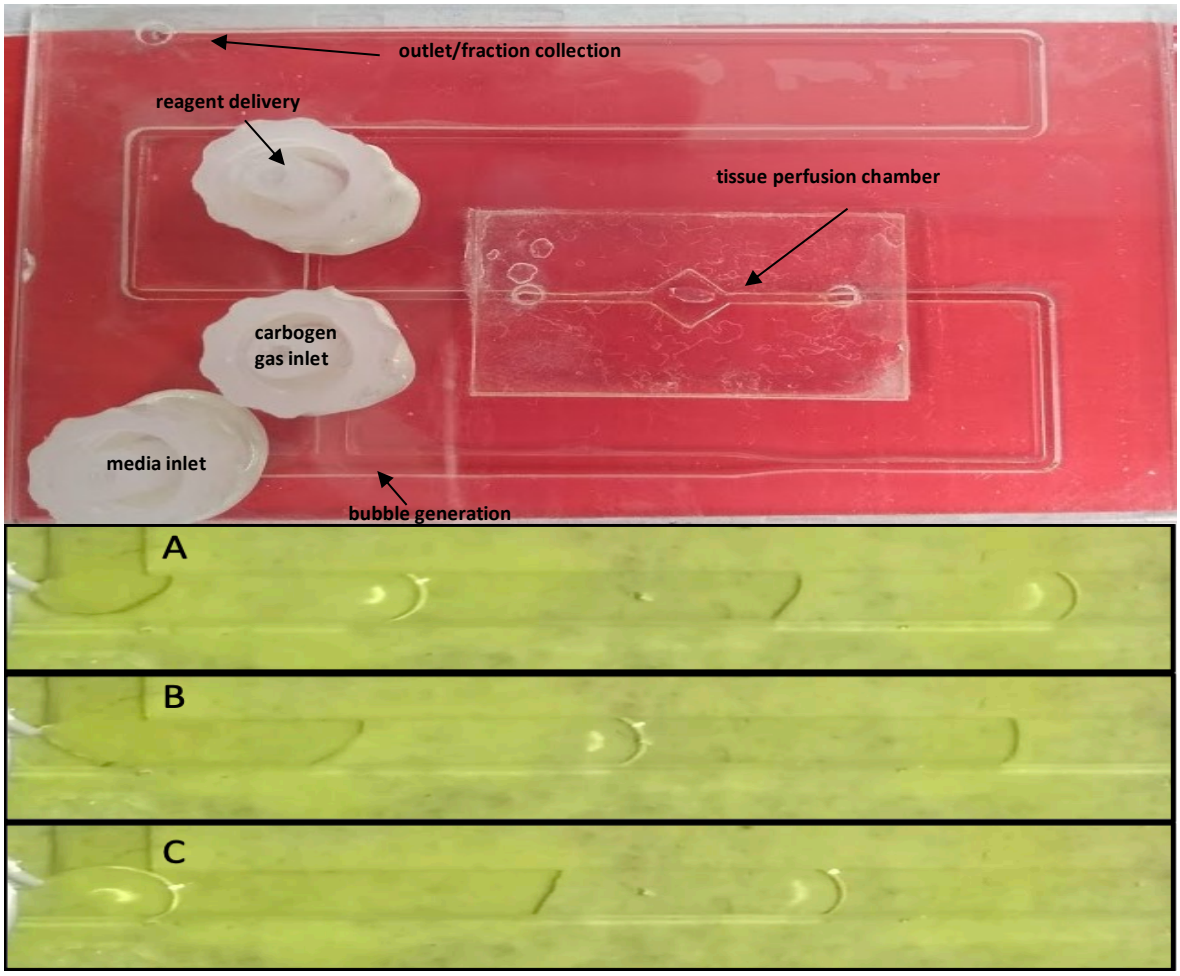

Figure 2-1. *Original microfluidic perfusion device*. Original device with T-junction demonstrating squeezing regime showing a droplet's a) filling of the junction b) expansion into the channel and c) scission.

2.2 Materials & methods

2.2.1 Materials and reagents

Agarose, fluorescein disodium salt, sodium chloride, potassium chloride, disodium phosphate, monopotassium phosphate, Sylgard® 184 silicone elastomer base and curing agent, and acetone were purchased from Thermo Fisher Scientific (Waltham, MA). GelBond® film was purchased from Lonza (Morristown, NJ). A miniature pneumatic solenoid valve (model no. 20) was purchased from Parker Hannifin Corporation (Cleveland, OH). All 3D printing was done with the Anycubic Photon S LCD-based SLA 3D printer from Anycubic 3D printing (Commerce, CA). LabVIEW (National Instruments, Austin, TX) was used to automate the system. ImageJ (National Institutes of Health, Bethesda, MD) was used for image analysis.

2.2.2 Droplet Generation

Method 1.0. Continuous flow of aCSF droplets segmented with carbogen gas improves oxygen and nutrient exchange into brain tissue slices while also allowing for time resolved measurement of perfusate droplets. However, perfusion volumes are dependent on flow rates of these droplets. The volume of a droplet is dependent on its length and width, both dimensions which are directly proportional to the ratio of flowrates of carbogen gas and aCSF in the squeezing regime used to produce these droplets. Reducing the volume of perfusate droplets would decrease the dilution of secreted biological molecules. The T-junction used in the previously developed microfluidic device was replaced by a single inlet connected to a miniature pneumatic solenoid valve. A waveform generator was used to supply 5V square wave pulse in order to power the valve and a n-channel metal-oxide-semiconductor field-effect transistor (MOSFET) was used in a circuit constructed to control the valve. Unlike like the squeezing regime used previously, the duty cycle of the square wave signal was easily manipulated to change the size of the bubbles and droplets. By using a duty cycle of 50% and making the flowrates of the gas and buffer equivalent, droplets and bubbles of equal volume were produced as seen in Figure 2-2. The pressure of the gas was set using the regulator valve on the tank then using the tubing dimensions, the flowrate of the gas was determined by the Hagen-Poiseuille equation (Eq.4):

$$\Delta p = \frac{8\mu L Q}{\pi r^4} \qquad (4)$$

Where Δp is the pressure loss, μ is the dynamic viscosity, L is the length of the tubing, Q is the volumetric flowrate and r is the radius of the tubing. The pressure needed for the buffer to match the flowrate of the gas was then calculated by plugging in the flowrate of the gas and solving for the Δp. Hydrostatic pressure was used to create the equivalent flowrate for the buffer, allowing droplets and bubble of equal volume to be generated.

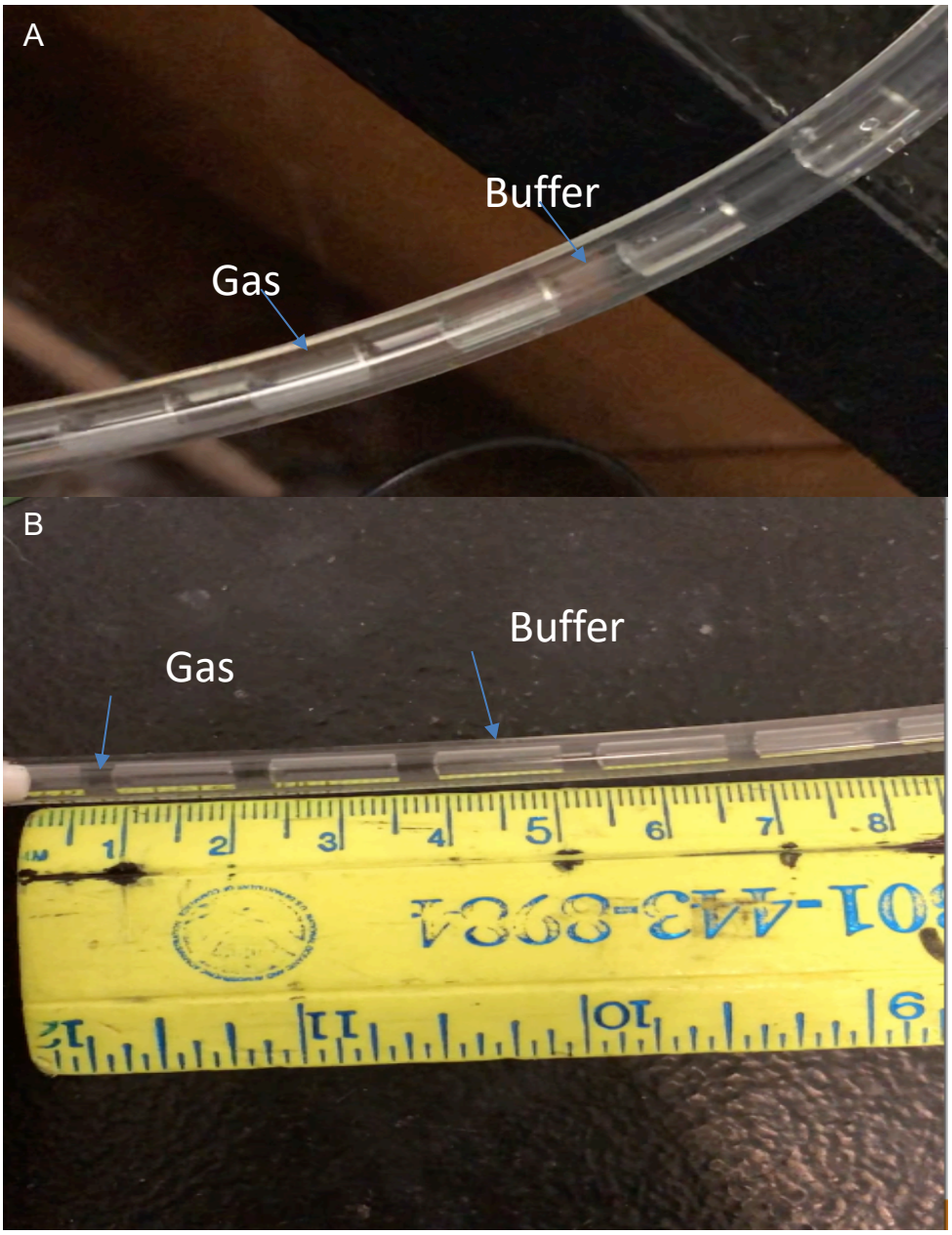

Figure 2-2. *Droplet Generation*. Continuous flow of droplets and bubbles generated using method 1.0 with varying size at a) 50% duty cycle and b) 30% duty cycle.

Method 2.0 To reduce the volume of droplets even further, a new method to introduce the droplet to the slice in the chamber was developed. This droplet delivery protocol enabled control of single droplet generation, effectively decreasing perfusion volume. Using a LabView program, a DAQ, and multiple solenoid valves, the entry of droplets and bubbles into the chamber was controlled, instead of continuously flowing. Using separate channels, the valve connected to a syringe containing aCSF is opened and a droplet is pushed through the channel to the chamber housing the tissue slice. That valve is then closed, stopping flow and effectively holding the droplet in the chamber until flow is started again. Next, the valve connected to the gas cylinder containing the carbogen gas is opened and a bubble flows through the channel to the chamber, pushing the droplet out. The valve is then closed, stopping flow and leaving the slice in the chamber surrounded by gas. All valves are connected to a simple switch circuit programmed to send a 5V signal for a fixed amount of time to open and close the corresponding valve at the touch of a button. By controlling when and how long either aCSF or carbogen is flowing through the perfusion device, the volume of the droplet can be reduced to the minimum volume needed to fill the chamber.

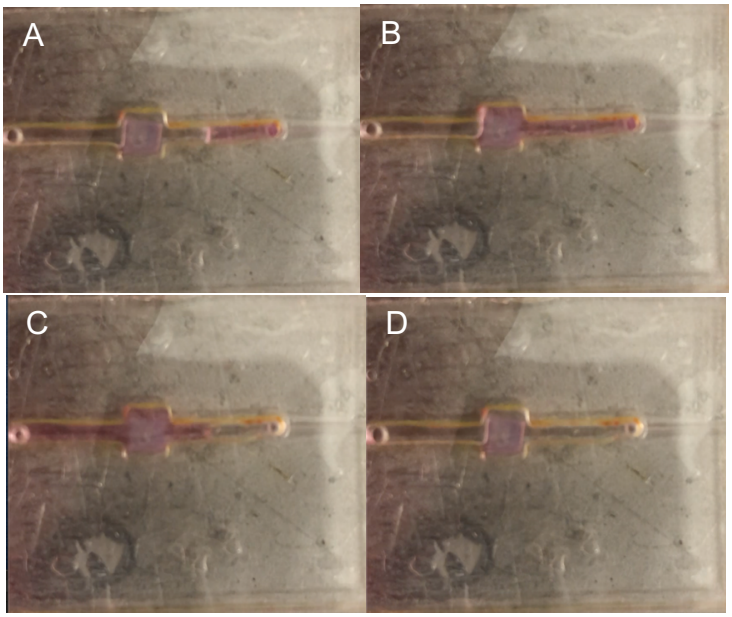

Figure 2-3. *Droplet delivery.* Frame by frame of a) a droplet entering the channel when the buffer valve is open b) flow stopping and the chamber being filled when the buffer valve is closed c) a droplet being pushed out of the chamber by a bubble when the gas valve is open d) flow stopping and the channel being filled with gas.

2.2.3 Device Fabrication

Chip 1.0 Holes were carefully drilled into a glass microscope slide for the inlets and outlets of the channels. Another microscope slide was then heated to approximately 300℃ over an open flame before the channels were etched into the surface of the glass using a laser-cutter. Once the channels were etched into the surface the microscope slide was transferred from the open flame to a hot plate where the temperature was maintained at 300℃ for at least 20 minutes. The hot microscope slide was then transferred to the oven to slowly cool down to room temperature overnight. The cooled microscope slide and the microscope slide with holes drilled into it were then plasma cleaned and aligned to form an airtight seal.

Chip 1.1 A mold of the same channel design as chip 1.0 was created in AutoCAD and 3D printed using the Anycubic Photon S 3D printer. Polydimethylsiloxane (PDMS) was then created using Sylgard 184. A 10:1 mixture of base elastomer to curing agent was poured into the 3D printed mold. To remove any air bubbles from the mixture, the mold was placed in a vac and left to set overnight.

Chip 1.2 A two rectangles with the dimensions of a standard microscope slide were laser-cut from poly(methyl methacrylate) (PMMA). Holes for inlets and outlets were drilled into the first piece while channels were etched into the second piece using the laser-cutter. A couple of drops acetone were added to the surface of each PMMA then they were aligned and clamped together with large binder clips until the acetone evaporated and a seal formed.

Chip 2.0 The same method was used as for chip 1.2, except all channels meet at a right angle, to reduce mixing of buffer and stimulant, rather than an angle less than 90° as seen in previous chips. The channel measure approximately 500μm wide and 300μm deep (Figure 2-5).

Chamber Housing. The chamber that houses the brain tissue slice was made of a combination of VHB tape and GelBond®. Two layers of VHB tape were combined to make the total height of the chamber approximately 3mm. The chamber was then laser-cut into the VHB tape. The cut tape was applied directly to the surface of the chip after aligning the inlets and outlets of the channels and chamber. GelBond® was added to the top of the chamber, with the hydrophilic side facing down, to close the chamber.

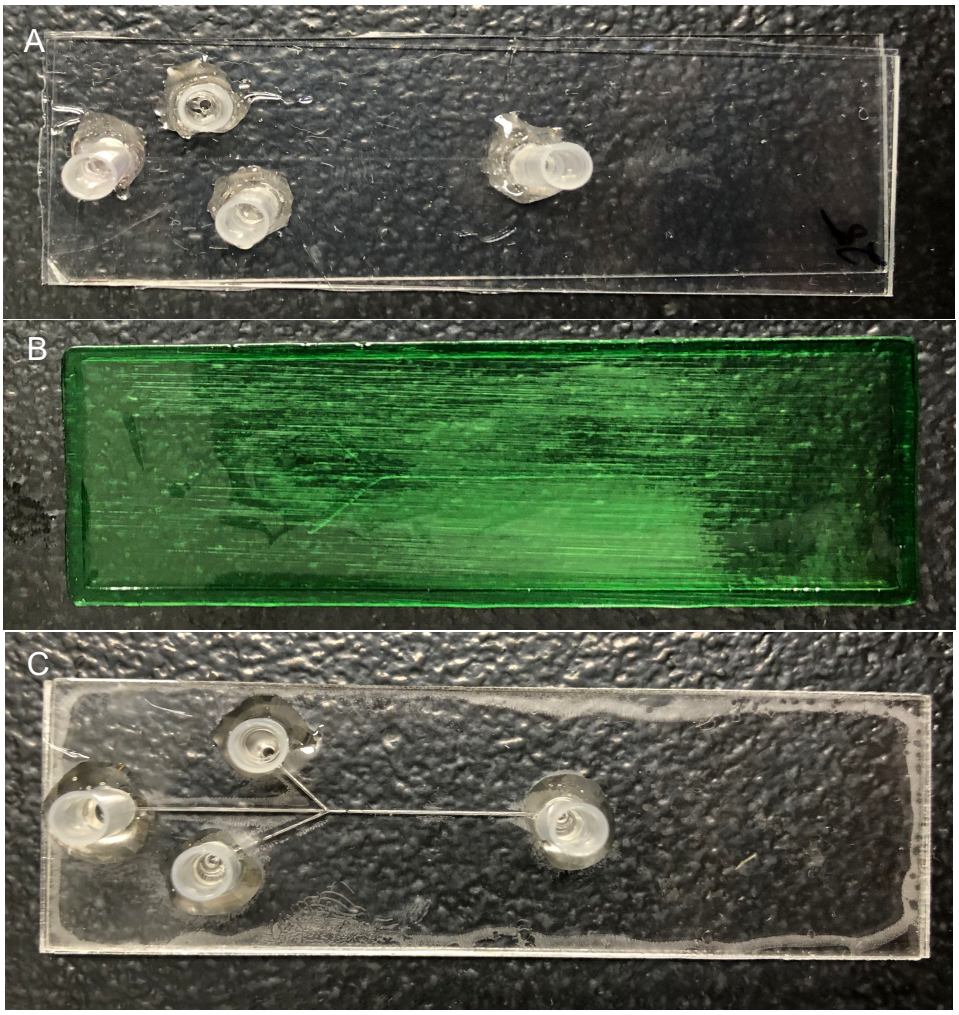

Figure 2-4. *Fabricated microfluidic devices*. a) chip 1.0 made using glass microscope slides b) chip 1.1 made of PDMS sitting in the 3D printed mold c) chip 1.2 made of PMMA bonded by acetone.

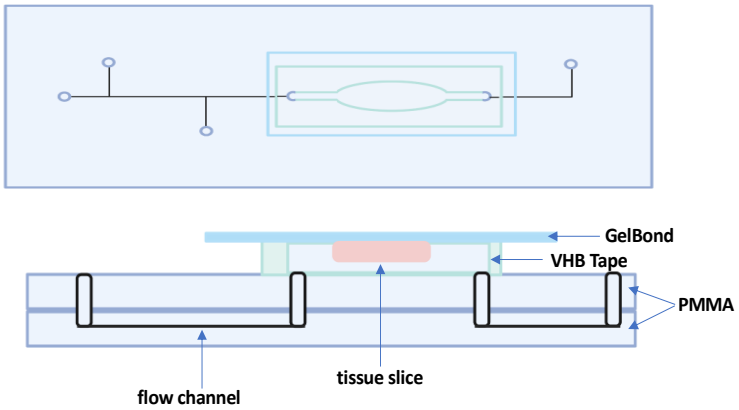

Figure 2-5. *Microfluidic bubble perfusion device.* Schematic of chip 2.0 with the chamber for a brain tissue slice.

2.3 Results & discussion

2.3.1 Droplet Generation

Method 1.0 Using a single solenoid valve at a single inlet to generate droplets and bubbles did allow for smaller volumes and proved to be superior to the original T-junction and squeezing regime, however, the method only worked when using phosphate-buffered saline (PBS). When using 100uM fluorescein in PBS buffer the droplets were no longer monodispersed at smaller volumes. The observed irregularity of the fluorescein droplets, seen in Figure 2-6, is likely due to the size and charge of the organic dye. The droplets seemed to be “sticking” to the walls of the tubing when leaving the valve and before entering the channel. This suggests that the fluorescein added to the solution increased the overall dynamic viscosity of the fluid. This increase in dynamic viscosity makes the fluorescein droplets more resistant to the pressure used to drive flow from the solenoid valve through the tubing. The pressure is great enough to readily overcome this resistance at the tubing’s axis more so than at the walls so droplets “stick” as these forces compete, until there is enough buildup of pressure to push the fluid some distance. The flowrate of the liquid versus the gas could have been calculated with this new dynamic viscosity and the setup could have been adjusted account for this but this method was not pursued further due to the initial inability to produce monodispersed droplets. Even if the

flowrates were corrected and the monodispersed droplets achieved with just PBS were duplicated, a new method was developed that reduced droplet volume even further. This new approach was ideal because future experiments would involve fluorescein and other organic molecules in order to image the system and verify slice viability in the chamber. Eliminating the use of a single solenoid valve reduced droplet volumes even further, while simultaneously improving tissue analysis.

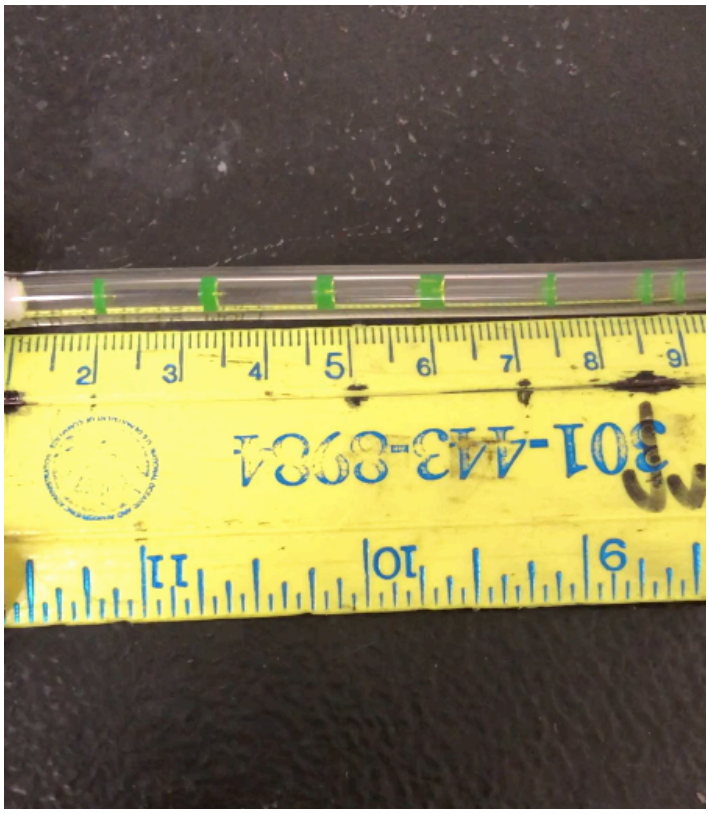

Figure 2-6. *Fluorescein droplets*. Small volume droplet of 100uM fluorescein in PBS buffer produced by Method 1.0 that are not uniform in size and spacing.

Method 2.0 The whole system was automated using LabVIEW and continuous flowing droplets were replace by single droplets delivered at a specified time. This method reduced the overall droplet volume because the minimum droplet volume needed is dependent on the chamber volume. Previous work showed that droplet volumes need to be greater than half the chamber volume and the chamber surface should be mostly hydrophilic to prevent droplets from breaking up in the chamber and being overtaken by the next droplet. A comparison of chamber shape, size and surface can be made to optimize the tissue slice housing. Square, diamond, and oval chamber shapes were designed in three varying sizes that would each be able to house a suprachiasmatic nucleus (SCN), hypothalamic, or whole mice brain slice. The contact angles of a water droplet on the surface of various materials were also measured. The effectiveness of any combination of all of these factors could be test by passing a single fluorescent droplet through the chamber, followed by droplets of buffer. The fluorescence intensity of the buffer droplets could be measured to quantify how much carryover is left between droplets. The ideal combination of chamber shape size and surface tension would have the least amount of carryover or the lowest measured fluorescence intensity.

Keeping droplets segmented by bubbles is important in obtaining temporal information from the molecules secreted by the tissue slice. By reducing the chamber size to the minimum volume needed to house a specific size brain tissue slice, the volume of a single droplet can also be reduced, and the dilution of the molecules secreted into media is limited.

2.3.2 Device Fabrication

Though the small volume channels of chip 1.0 were desirable to the overall design of this microfluidic device, they were not functional. The back pressure within the channels was so great that it was impossible to pump droplets into the device even when using a syringe pump. The fabrication process was also tedious and yielded less than 50% of viable chips. This was due to the glass frequently cracking while cooling to room temperature from experiencing thermal stress. While the glass was heated close to its melting point in an attempt to reduce its amorphous nature, the cooling process still happened too quickly. The rapid changes in temperature induced stress on the surface of the glass chips and cause cracking along the etched channels.

The PDMS mixture used to make chip 1.1 never set properly after numerous attempts. The polymer remained tacky and never fully solidified. This is thought to be a result of the 3D printed mold inhibiting the PDMS from curing properly due to compounds in the resin, such as uncured monomers and photo-initiators, leaching from the printed parts. Strategies to overcome this limitation, such as coating the printed devices, have been proposed by others experiencing this

problem.[33] However, this method was not pursued further because smaller channel dimensions were possible through other fabrication methods.

While PMMA is sometimes called acrylic glass, it is a tough plastic polymer used as a glass alternative. Unlike glass, channels could be etched into the surface of the PMMA without heating or cracking the material because it has a much lower melting point and does not experience the same thermal stress. Chip 1.2 and 2.0 were easily reproduced and the whole fabrication process could be completed in less than an hour. Droplets were easily flowed through the channels and the chips were reusable. The chamber housing could easily be placed on and removed from the surface of the PMMA device.

CHAPTER 3. COMSOL SIMULATIONS FOR UNDERSTANDING LATERAL ELECTROPHORESIS

3.1 Introduction

Electrophoretic methods such as isoelectric focusing and isotachophoresis have been used for sample enrichment in capillary electrophoresis, as well as in microfluidic devices.[34,35] Generally, in these electrophoretic preconcentration techniques, the capillary is divided into sections by a discrepancy in a property, like pH or conductivity of solution.[34] Long sample bands can be compressed into narrow, concentrated zones, by choosing appropriate conditions to manipulate analyte migration times in the capillary.[34]

In the developed microfluidic bubble perfusion device, the size of the tissue slices, and the dimensions required to house the slice in the chamber present a lower limit of droplet volume on the order of 10μL. In order to increase the concentrations of molecules of interest within perfusate droplets and improve downstream assay of cellular secretions, sample preconcentration is needed. An electrophoretic preconcentration method was developed to be incorporated into the microfluidic bubble perfusion device.

The developed electrophoretic platform utilizes platinum electrodes inserted in the sides of the channel within the microfluidic device. An electric potential is applied to the electrodes and as the perfusate droplets flow down the channel and through the electrodes, molecules concentrate at the electrode of opposite charge via lateral electrophoresis. The concentrated molecules at either electrode are separated further down the channel, reducing the overall volume. Proof-of-concept experiments were completed using 100 µM fluorescein in PBS. Platinum electrodes were integrated into the walls of the flow channels, and initially electric fields of 4, 8, 24, and 40 Vcm^{-1} were applied. In Figure 3-2, the buffer solution can be observed boiling in the channel due to joule heating before any separation occurs in electric fields higher then 4 Vcm^{-1}. Two Peltier coolers were stacked and placed directly below the channel of the microfluidic device in order to combat the effects of joule heating. The experiments were repeated and electric fields from 30 to 50 Vcm^{-1} were reached with no signs of joule heating. Fluorescence imaging was used to confirm the concentration of fluorescein to one side of the channel by comparing the fluorescence intensity across the channel before and in between the electrodes. Images showed fluorescein concentrating at the negatively charged electrode. Fluorescein is a negatively charged molecule and therefore was expected to be observed concentrating at the positively charged electrode. It is hypothesized that the smaller anions and cations present in the buffer migrate through the electric field and to the electrodes at a much faster rate than the larger fluorescein molecules, causing ion concentration polarization.

In Figure 3-2, 100 μM fluorescein was flowed continuously through the channel of the developed electrophoretic platform. As the electric field was increased, the solution could be observed boiling in the channel due to joule heating. This was corrected with Peltier coolers, used to reduce the overall temperature in the channel while an electric field is applied. In Figure 3-3, droplets are seen flowing through the channel with and without the Peltier coolers. Without the thermoelectric cooling devices, most the solution is boiled of before exiting the channel, whereas, with the devices, no boiling is observed within the channel, even when a higher electric field was applied.

In Figure 3-4, 100 μM fluorescein was flowed through the channel that is being cooled by Peltier coolers. The use of the Peltier coolers keeps the channel at low temperatures, preventing joule heating and allowing higher electric fields to be applied. Images of the fluorescein flowing through the channel were obtained and analyzed using ImageJ. By measuring the relative fluorescence intensity of the channel, the accumulation of fluorescein at the electrode was confirmed. Surface plots show high fluorescence intensity on the right side of the plot, which corresponds to the concentration of fluorescein flowing through the channel before reaching the electrodes. The left side of the surface plots only show fluorescence intensity towards the top plot corresponding with the accumulation of fluorescein on the top electrode. In all three of the electric fields shown, the corresponding surface plots confirms the accumulation of fluorescein at the top electrode.

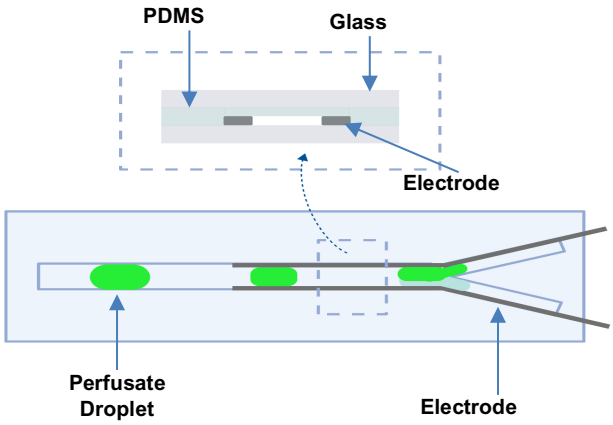

Figure 3-1. *Schematic of electrophoretic platform.* Schematic with cross section of microfluidic channel for lateral electrophoresis

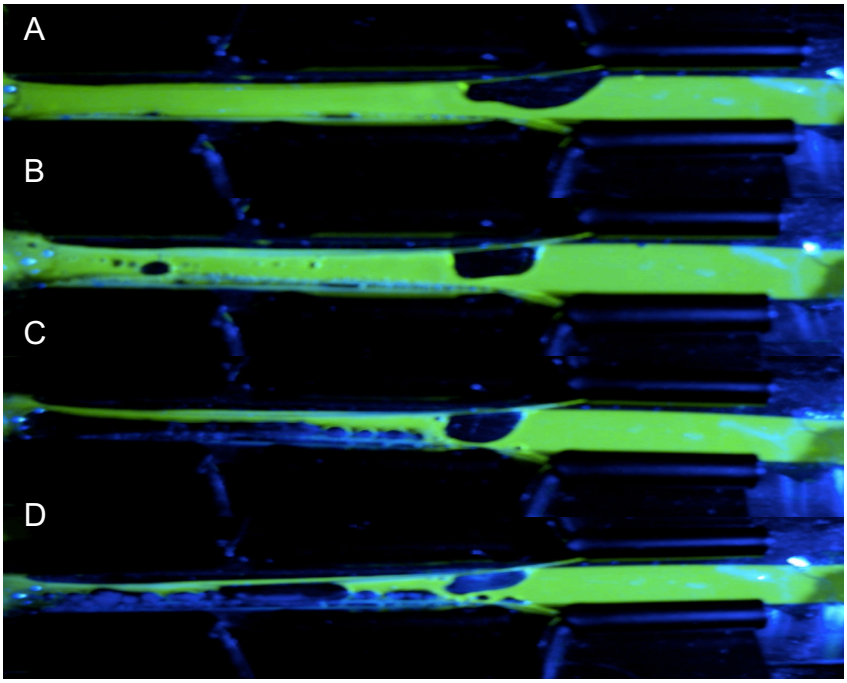

Figure 3-2. *Original lateral electrophoresis experiment.*100 μM fluorescein flowing continuously through the electrophoretic channel from right to left in electric fields of a) 4 Vcm^{-1} b) 8 Vcm^{-1} c) 24 Vcm^{-1} d) 40 Vcm^{-1}.

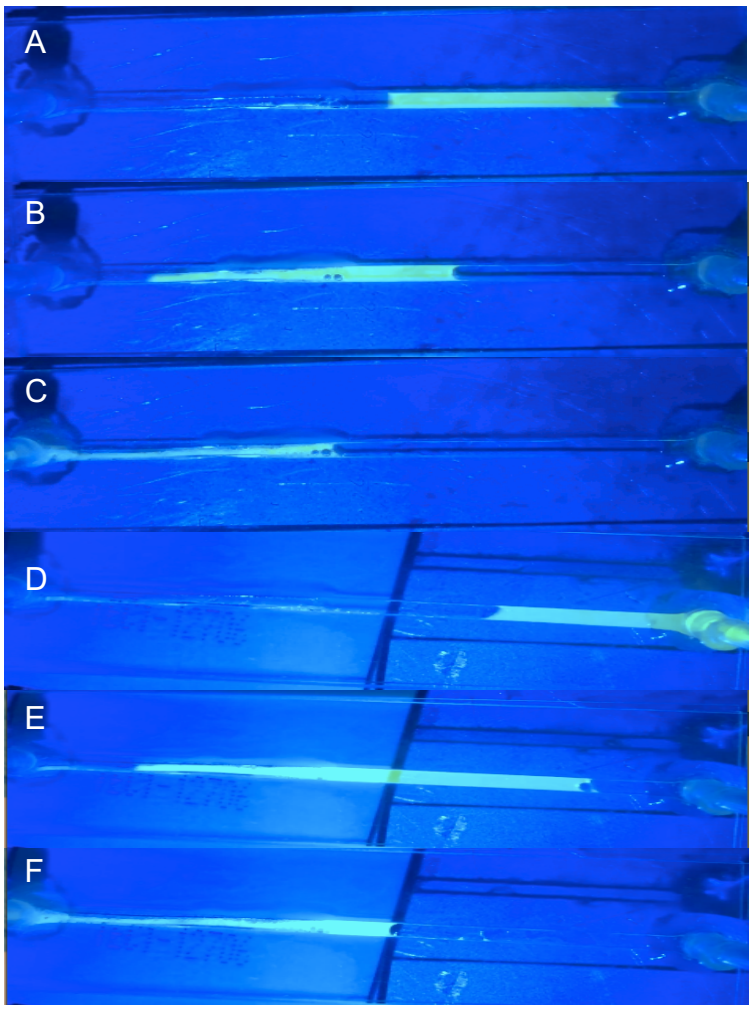

Figure 3-3. *Thermoelectric cooling*. Droplets of 100 μM fluorescein in an electric field of 50 Vcm^{-1} a) entering the channel b) entering the electric field c) exiting the channel, without Peltier coolers; d) entering the channel e) entering the electric field f) exiting the channel, with Peltier coolers.

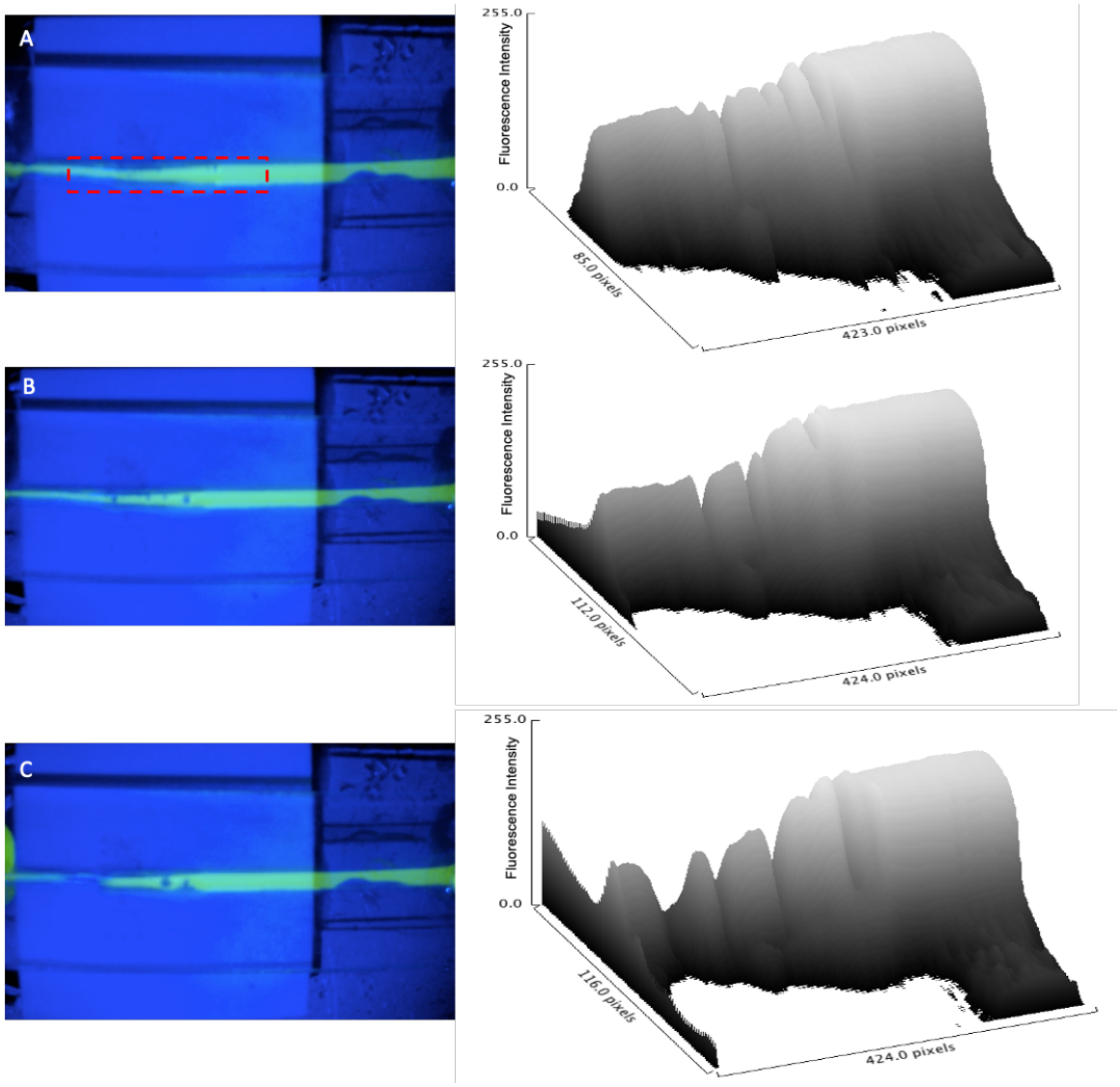

Figure 3-4. *Lateral electrophoresis with Peltier coolers*. 100 μM fluorescein flowing from right to left in a) 30 Vcm^{-1} b) 40 Vcm^{-1} c) 50 Vcm^{-1} electric fields with Peltier coolers to correct joule heating. The dashed red line shows the area of the image used to make the corresponding surface plot, confirming the migration of fluorescein to the negative (top) electrode.

Lateral electrophoresis was then simulated using COMSOL Multiphysics in an effort to better understand the observed behavior of these molecules and recreate the ion concentration polarization seen within the channel. When solving any problem using EOF in COMSOL, electric currents or electrostatics, creeping or laminar flow, and transport of diluted species are the three main physics involved in the simulation. Each solves for the potential, velocity and pressure, and concentration, respectively. The electric currents or electrostatics interfaces are similar, both requiring an electric potential to define and electric field (Eq 5).

$$E = -\nabla V \tag{5}$$

The equations in the electric currents interface are formulated with electrical conductivity(σ) (Eq. 6) and using boundary conditions, the electric potential can be specified at different locations to make electrodes with defined voltage, current, or power applied to drive the fluid motion.

$$J = \sigma E \tag{6}$$

Creeping or laminar flow is determined by the Reynolds number being greater than or less than one. The Reynolds number gives the ratio of inertial forces to viscous forces (Eq. 7):

$$R_e = \frac{\rho u_0 L}{\mu} \tag{7}$$

Where the inertial force is ρ, the density of the fluid, u_0, the velocity of the fluid, and L, the width of the channel and μ is the dynamic viscosity of the fluid. When the Reynolds number is less than one the inertial force becomes negligible allowing the term to be ignored when solving for the Navier-Stokes equation. The flow will be pressure-driven and solving the Eq 8. will define the parabolic flow profile.

$$\rho\left(\frac{\partial \vec{u}}{\partial t} + \vec{u} \cdot \nabla\vec{u}\right) = -\nabla p + \mu\nabla^2\vec{u} + \vec{f} \tag{8}$$

When using electroosmotic flow the inlets and outlets are defined as having an absolute pressure of 1 atm and the zeta potential (ζ), electric field (E_t), and

relative permittivity ($\in_r$) are used to calculate the electroosmotic velocity (u_{slip}) at the walls of the channel (Eq 9.).

$$u_{slip} = \frac{-\in_r \in_0 \zeta}{\mu} E_t \quad (9)$$

The last physic, transport of dilute species, accounts for diffusion, convection and/or migration of the species. The Nernst-Planck Equation embodies all three modes of transport (Eq 10.):

$$J_i = -D_i \nabla C_i + \frac{-Z_i^F}{RT} D_i C_i \nabla \phi + C_i v \quad (10)$$

Where is flux of the species, is the diffusion coefficient, is the concentration of the species, is the potential and is the velocity of the species. The first term is diffusion, the second term is migration and the third term is convection. Convection is just fluid motion carrying the species and is based on the fluid flow conditions from the creeping/laminar flow solution, so in the case of EOF the electroosmotic velocity from the creeping flow solution is carried to the convection term in Eq 10.

3.2 Materials & methods

3.2.1 Materials and reagents

Fluorescein disodium salt, sodium chloride, potassium chloride, disodium phosphate, and monopotassium phosphate were purchased from Thermo Fisher Scientific (Waltham, MA). PDMS (250μm) was purchased from Stockwell Elastomerics (Philadelphia, PA). COMSOL Multiphysics simulations were performed using a Dell Precision Tower 7810 Workstation. ImageJ (National Institutes of Health, Bethesda, MD) was used for image analysis.

3.2.2 Band Dispersion in EOF

Using COMSOL Multiphysics, a model of the dispersion of a neutral species band in EOF moving through a curved microfluidic channel was simulated. Electric currents, creeping flow, and transport of diluted species were the three physics used to solve this problem. The velocity field from creeping flow was coupled to the transport properties and convection was the mechanism by which the species moved through the channel.

3.2.3 Simulating Electrophoresis

The simulation used to study the dispersion of a neutral species band in EOF was used as a base model for simulating electrophoresis. The transport mechanism was changed from convection to migration in an electric field in order to assign a charge to species and another concentration was added. Differing charges were assigned to the two concentrations in order to observe an electrophoretic separation. All other physics remained the same as the original model.

3.2.4 Simulating Lateral Electrophoresis

From there, the same physics were used to simulate the phenomenon that was being observed in the electrophoretic channel. Properties, such as density, concentration, and relative permittivity, of PBS were plugged in as parameters in the simulation and an electric field of $50 Vcm^{-1}$ was simulated to mimic the real-life experiments that were already conducted. A stationary and time dependent study was run for this simulation.

3.3 Results & discussion

3.3.1 Band Dispersion in EOF

The velocity magnitude within the curved microchannel and be observed in Figure 3-5. It remains uniform in the straight paths of the channel but there is an increase in velocity on the inner curve and a decrease in velocity on the outer curve. This velocity gradient causes dispersion as the band of neutral species travels around the curve. Molecules closer to the inside of the curve are accelerated for a fraction of the migration time while molecules closer to the outside are decelerated. Even though the velocity once again becomes uniform further down the channel, after the curve, the band continues to disperse because molecules arrive to this uniform point in the channel at different times, as shown in Figure 3-6.

The mechanism of transport of species for this simulation was convection. The species in this problem is neutral so it was not necessary to use migration in an electric field as the mechanism of transport. Even though it does not use a charged species, this simulation was used as the base model for simulating electrophoresis because of the use of EOF.

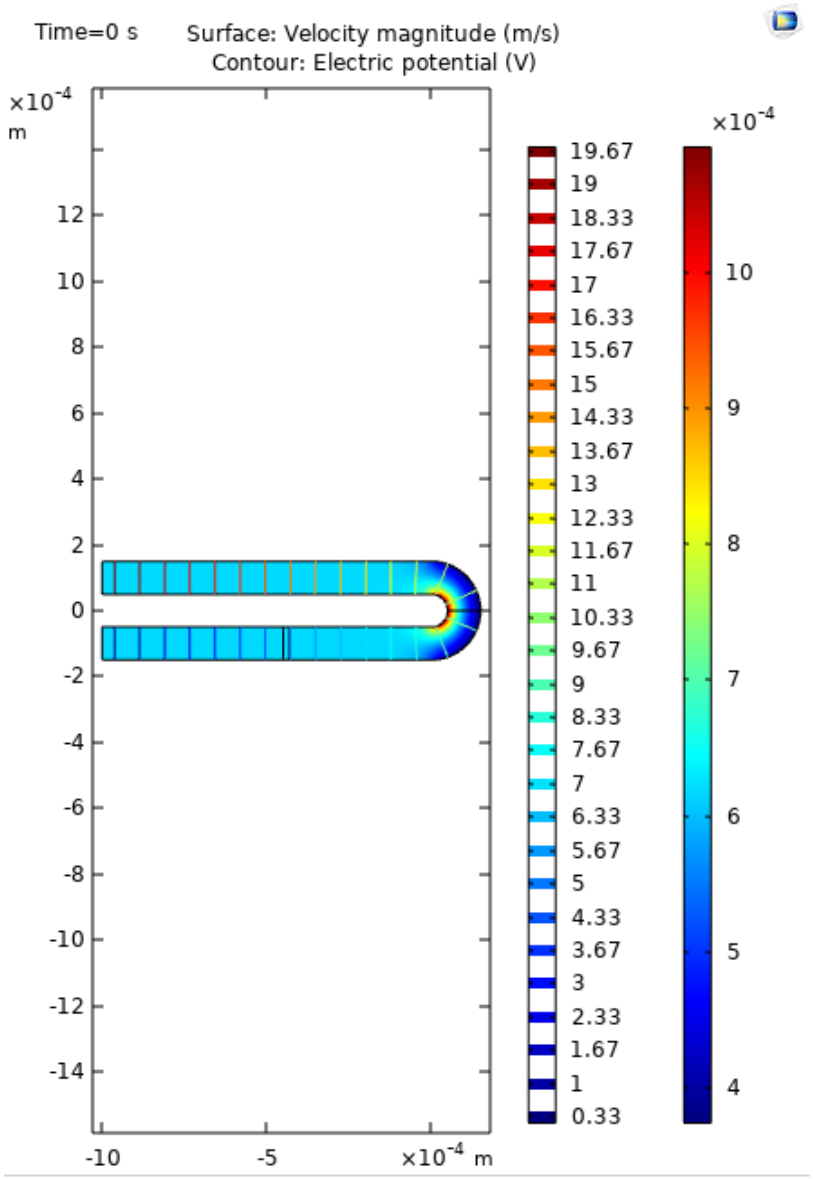

Figure 3-5. *Velocity and electric potential.* Surface plot of the velocity magnitude and electric potential throughout the microchannel.

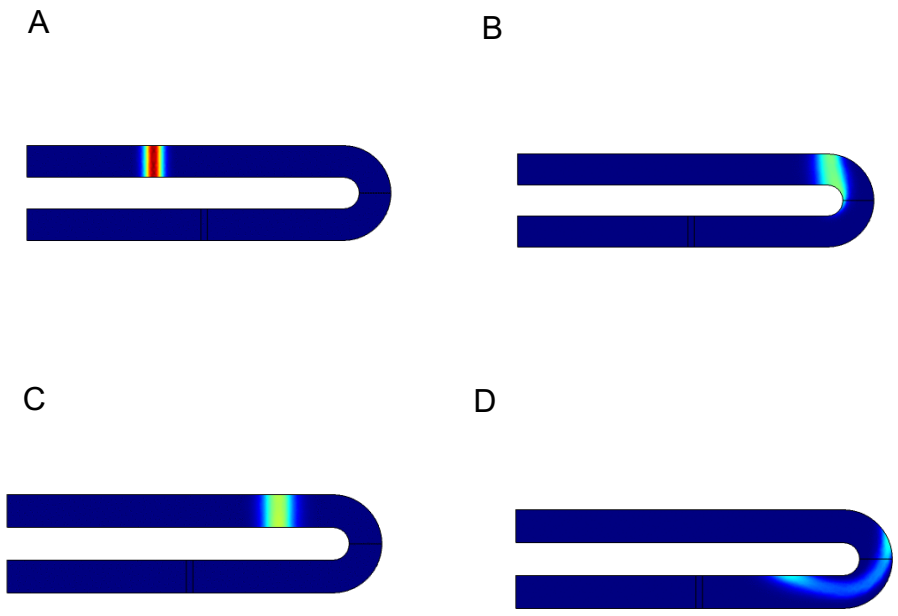

Figure 3-6. *Band dispersion*. Neutral species band in EOF moving through a curved microchannel at a) 0s b) 0.5s c) 1s d) 1.4s

3.3.2 Simulating Electrophoresis

In order to simulate electrophoresis, the same parameters and boundary conditions from the previous problem were used. The mechanism of transport was changed from convection to migration in an electric field in order to add a charge to the species. A second species with the same concentration and a different charge was added. The electric potential and velocity magnitude also remained the same as previously shown in Figure 3-5.

Figure 3-7 shows two species, one with a negative charge and one with a positive charge, moving away from each other. The electric field carries the negatively charged species to the left while carrying the positively charge species to the right. In Figure 3-8, the two species are moving in the same direction, to the right, because they are both positively charged. However, the separation can still be observed because there is a difference in migration time due to the difference in magnitude of charge. The species with the charge of greater magnitude travels through the channel faster, as expected.

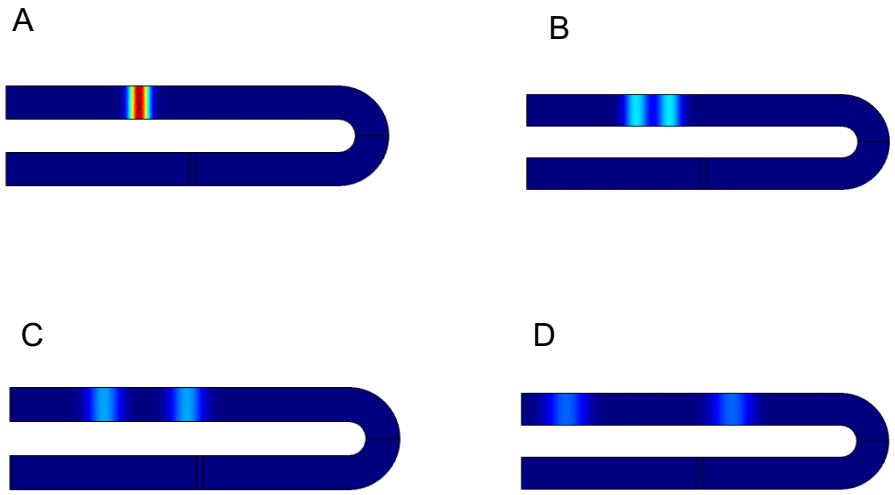

Figure 3-7. *Electrophoretic separation 1.0*. Species with -1, traveling to the left, and +1 charge, traveling to the right at a) 0s b) 27s c) 44s d) 80s.

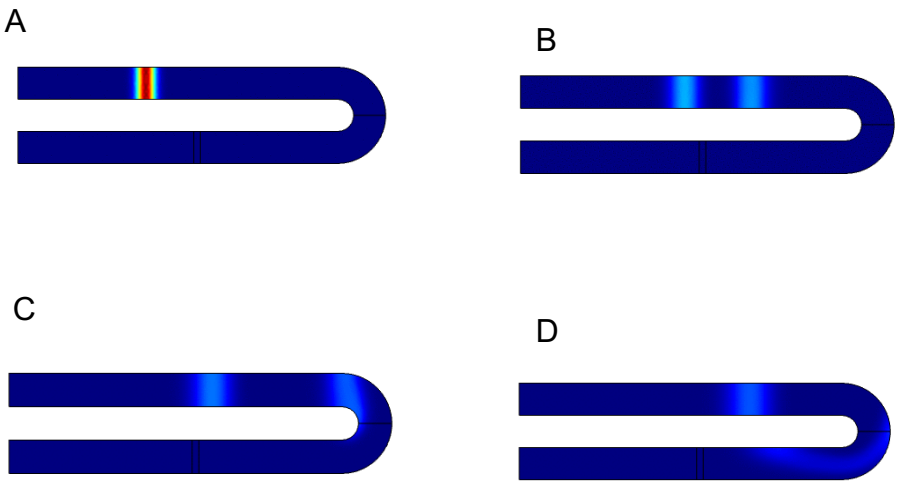

Figure 3-8. *Electrophoretic separation 2.0*. Species with +3 and +1 charge, both traveling to the right at a) 0s b) 31s c) 60s d) 88s.

The electrophoresis simulation happens on a larger time scale than the dispersion of the neutral species band. This suggests that pressure driven flow is a faster method for moving species through a microchannel. However, even when including species of differing charges, pressure drive flow does not yield the separation needed within the developed microfluidic device.

3.3.3 Simulating Lateral Electrophoresis

Using the same physics as the two previous simulations, the microchannel used in proof-of-concept experiments was modeled. The flow in the channel from right to left can be seen illustrated in the surface plot in Figure 3-9, as well as the electric potential from the $50 Vcm^{-1}$ electric field. The whole channel was not modeled, instead just the portion right before the electrodes and slightly after the electrodes.

When looking at the surface plot of the concentration from the stationary study, it initially looks as if there is no concentration in the channel at all. Upon closer inspection, zooming in on the electrode, the species can be seen concentrated on the surface of the negative electrode. For this simulation, the mechanism of transport is also migration in an electric field and the species observed in Figure 3-10 was given a positive charge to simulate the cations within the buffer solution. The concentration of cations at the negative electrode in the stationary study of this simulation support the hypothesis that the charge ions within the buffer solution concentrate on the electrode of opposite charge, before the fluorescein molecules travels through the electric field. The time dependent study reflects this also, showing an increase in the concentration of cations at the negative electrode as time elapses. The slight depletion of concentration at the opposite electrode can also be observed. This suggest that if the charge of the species was reversed, it would concentrate at the opposite electrode and given two species with opposite charge, both electrodes would be an area of high concentration within the channel.

The results of the simulation do not directly reflect what was observed in the initial lateral electrophoresis experiments. The ion concentration polarization that caused the fluorescein to concentrate at the electrode of the same charge is not demonstrated in this simulation. The movement of the buffer ions to the opposing electrodes is simulated, however, the electric field produced by these ions concentrating in solution is not accounted for. To simulate the whole process of ion concentration polarization, the electrostatic effects produced by the high concentration of buffer ions at the electrodes would need to be appropriately modeled. The transport of diluted species physics is limited in the fact that it models diluted species that may become concentrated after transport but not the effects after that concentration. This model could be divided into two parts where the resulting electric field could be estimated, since it is known that it is strong enough to cancel out the initial electric field, and used to model the effects after

the buffer ions have concentrated but the accuracy of this second step could not be confirmed and would not be useful for predicting the behavior of other molecules besides fluorescein.

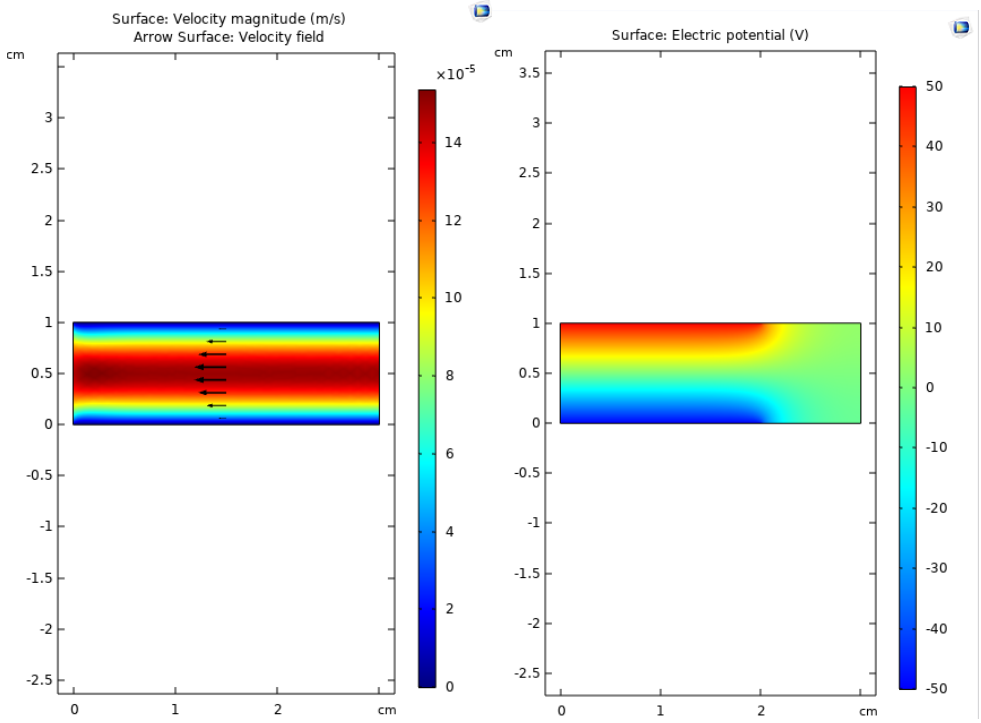

Figure 3-9. *Flow profile and electric potential.* Surface plots showing the velocity magnitude with flow profile and electric potential at and around the electrodes.

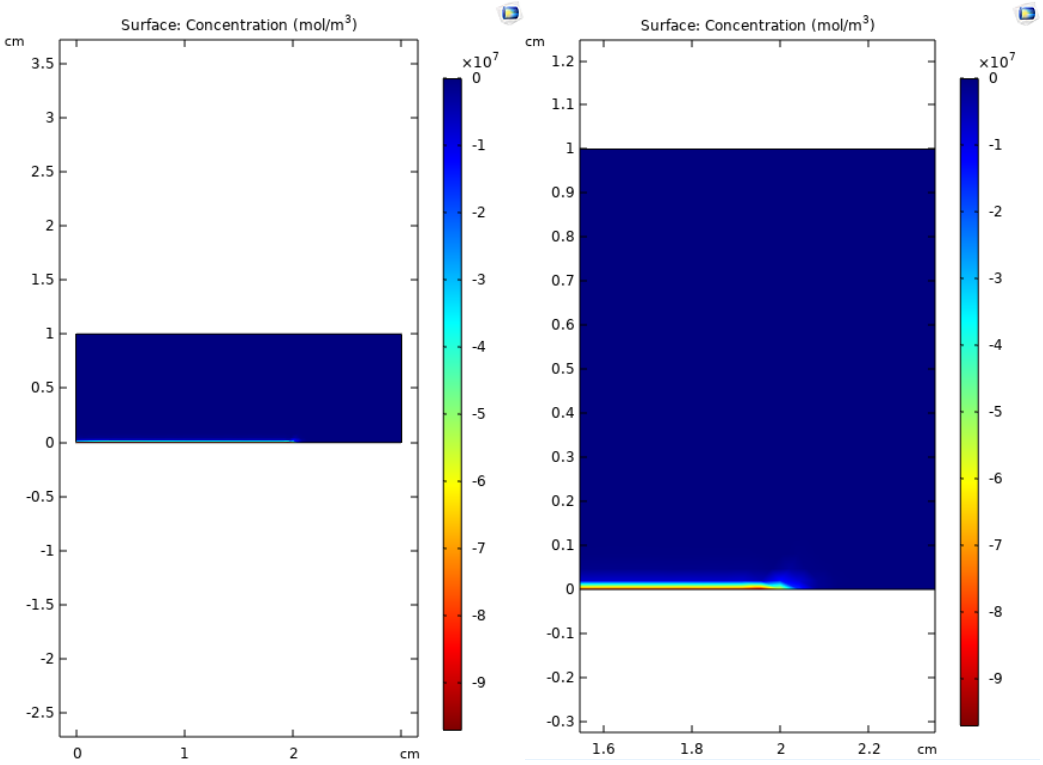

Figure 3-10. *Stationary study.* Surface plot of concentration throughout the channel with a closer look at the change in concentration on the right.

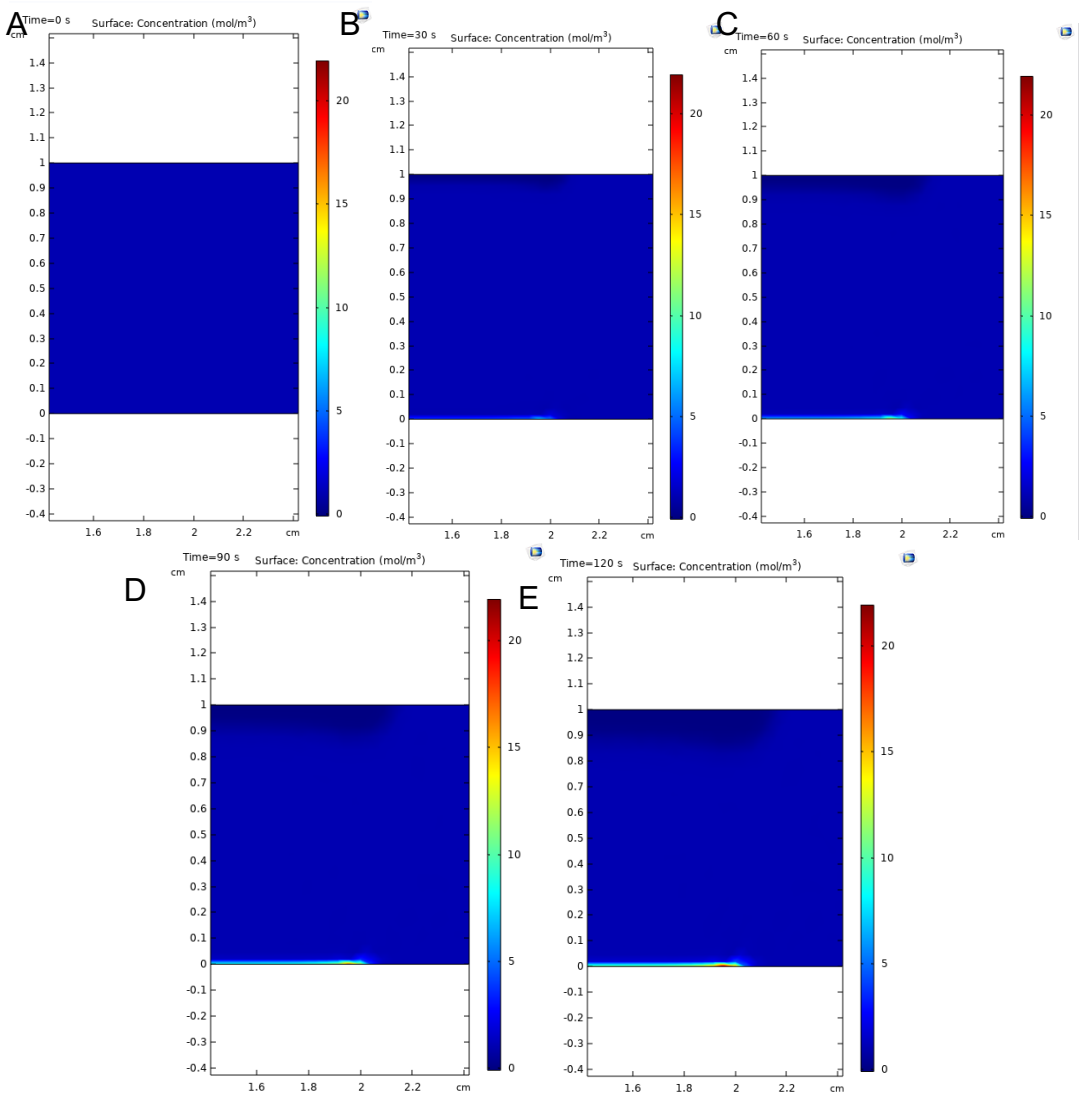

Figure 3-11. *Time dependent study*. Surface plots showing the increase and decrease in concentration at the electrodes at a) 0s b) 30s c) 60s d) 90s e) 120s.

CHAPTER 4. FUTURE DIRECTIONS

Studying the secretion dynamics of neuropeptides enables better understanding of endocrine mechanisms and regulatory relationships that may be involved in neurodevelopmental disorders like ASD. *Ex vivo* brain tissue slices are a useful model for studying these mechanisms, but conventional culturing techniques are poorly suited for imaging or chemical analysis. The culturing of organotypic brain slices can preserve brain structure and maintain the functionality of neurons within the sliced region while allowing control of the extracellular environment.[24,25] These *ex vivo* models are established tools to study basal and diseased state neurochemistry.[26]

The typical microfluidic device used to culture these slices uses continuous flow of aCSF and does not allow for time-resolved measurements of tissue secretions that contain biological molecules of interest due to the diffusional mixing of analytes between the time of secretion and collection of the perfusate samples. The device developed in chapter 2, generates monodispersed droplets ensuring the tissue slice spends equal amounts of time in media and oxygen thereby improving the exchange while also allowing for time resolved sampling.

Further development of both devices discussed in chapter 2 and 3 will deliver technologies that address existing shortcomings in the field of neuroendocrine characterization and brain tissue slice culture methodologies. With better understanding of the observe phenomenon in the developed electrophoretic channel, the preconcentration method can be incorporated to the microfluidic device developed in chapter 2. Successful integration will yield decreased dilution of sampled biomolecules in perfusate droplets for optimized downstream analysis.

Once the generation and collection and perfusate droplets has been optimized an immunoassay can also be integrated into the microfluidic device. Fluorescence anisotropy immunoassays have been described previously as a means for separation-free assay of secreted peptide hormones.[36] In this case, a separation-free approach is particularly attractive because it simplifies the integration of immunoassays with the segmented droplet flow system.

In fluorescence anisotropy a fluorescent sample is excited with linearly polarized light, and the degree of depolarization upon fluorescence emission is quantified to determine the relative rate of molecular rotation (Figure 4-1). In a fluorescence anisotropy immunoassay, a fluorescently labeled analog of the analyte of interest would be added to the sample solution along with the complementary antibody. The analyte of interest then competes with the fluorescently labeled analog to bind to antibody. With the increasing concentration of the analyte of interest, there would be an increase of free fluorescently labeled analog and a decrease

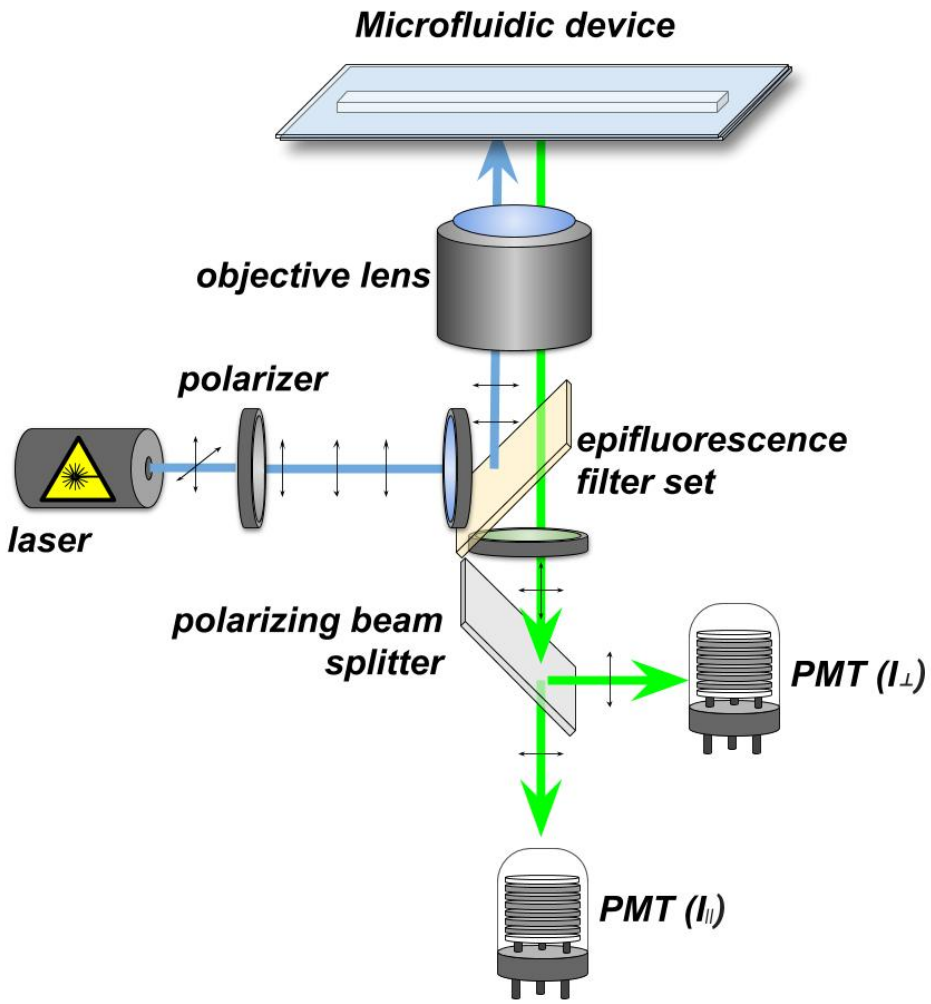

Figure 4-1. *Fluorescence anisotropy*. Schematic of fluorescence anisotropy optical setup

in labeled analog-antibody complexes as a result of binding competition. Since the rate of rotation of the fluorescently labeled analog is much greater than that of the labeled analog-antibody complex, the degree of free vs. bound fluorescently labeled analog can be determined via fluorescence anisotropy.[36]

Integrating the anisotropy immunoassay with the perfusion microdevice will require developing the microscope instrumentation. In this set up, excitation light is polarized via a polarizing filter before being subjected to the sample via conventional epifluorescence microscopy. Fluorescence emission is then collected and passed through a polarizing beam splitter to allow perpendicular polarized components to be detected at two separate photomultiplier tubes. The ratio of polarized signals (*r*) is used to determine the fluorescence anisotropy (Eq. 11):

$$r = \frac{I_{||} - I_{\perp}}{I_{||} + 2I_{\perp}} \qquad (11)$$

where $I_{||}$ is the intensity of fluorescence emission with identical polarization to the excitation source and $I_{\perp}$ is the intensity of fluorescence emission polarized perpendicular to the excitation source.[36]

The relationship between the analyte of interest concentration and *r* can be calibrated using commercially available standards in order to create standard curves to determine the concentration of each neuropeptides or other molecules of interest in collected perfusate droplets. The future of this project will develop the technologies needed to measure the time-resolved secretion of these neuropeptides at biologically relevant concentrations from *ex vivo* brain tissue cultures.

REFERENCES

(1) Green, J. J.; Hollander, E. Autism and Oxytocin: New Developments in Translational Approaches to Therapeutics. *Neurotherapeutics* **2010**, *7* (3), 250–257. https://doi.org/10.1016/j.nurt.2010.05.006.
(2) Won, H.; Mah, W.; Kim, E. Autism Spectrum Disorder Causes, Mechanisms, and Treatments: Focus on Neuronal Synapses. *Front. Mol. Neurosci.* **2013**, *6*. https://doi.org/10.3389/fnmol.2013.00019.
(3) Devlin, B.; Scherer, S. W. Genetic Architecture in Autism Spectrum Disorder. *Curr. Opin. Genet. Dev.* **2012**, *22* (3), 229–237. https://doi.org/10.1016/J.GDE.2012.03.002.
(4) Maenner, M. J.; Shaw, K. A.; Baio, J.; Washington, A.; Patrick, M.; DiRienzo, M.; Christensen, D. L.; Wiggins, L. D.; Pettygrove, S.; Andrews, J. G.; et al. Prevalence of Autism Spectrum Disorder Among Children Aged 8 Years — Autism and Developmental Disabilities Monitoring Network, 11 Sites, United States, 2016. *MMWR. Surveill. Summ.* **2020**, *69* (4), 1–12. https://doi.org/10.15585/mmwr.ss6904a1.
(5) Bonnet-Brilhault, F.; Tuller, L.; Prévost, P.; Malvy, J.; Zebib, R.; Ferré, S.; dos Santos, C.; Roux, S.; Houy-Durand, E.; Magné, R.; et al. A Strategic Plan to Identify Key Neurophysiological Mechanisms and Brain Circuits in Autism. *J. Chem. Neuroanat.* **2018**, *89*, 69–72. https://doi.org/10.1016/J.JCHEMNEU.2017.11.007.
(6) Romano, A.; Tempesta, B.; Micioni Di Bonaventura, M. V.; Gaetani, S. From Autism to Eating Disorders and More: The Role of Oxytocin in Neuropsychiatric Disorders . *Frontiers in Neuroscience* . 2016, p 497.
(7) Bartz, J. A.; Hollander, E. Oxytocin and Experimental Therapeutics in Autism Spectrum Disorders. *Prog. Brain Res.* **2008**, *170*, 451–462. https://doi.org/10.1016/S0079-6123(08)00435-4.
(8) Marieb, E. *Anatomy & Physiology*; Pearson Education, Inc.: Glenview, IL, 2014.
(9) Song, Z.; Albers, H. E. Cross-Talk among Oxytocin and Arginine-Vasopressin Receptors: Relevance for Basic and Clinical Studies of the Brain and Periphery. *Front. Neuroendocrinol.* **2018**, *51*, 14–24. https://doi.org/10.1016/J.YFRNE.2017.10.004.
(10) Armstrong, W. E. Vasopressin (AVP). *Encycl. Horm.* **2003**, 575–583. https://doi.org/10.1016/B0-12-341103-3/00299-0.
(11) Carter, C. S. Sex Differences in Oxytocin and Vasopressin: Implications for Autism Spectrum Disorders? *Behav. Brain Res.* **2007**, *176* (1), 170–186. https://doi.org/10.1016/J.BBR.2006.08.025.
(12) Insel, T. R.; O'Brien, D. J.; Leckman, J. F. Oxytocin, Vasopressin, and Autism: Is There a Connection? *Biological Psychiatry*. Elsevier January 15, 1999, pp 145–157. https://doi.org/10.1016/S0006-3223(98)00142-5.
(13) Miller, M.; Bales, K. L.; Taylor, S. L.; Yoon, J.; Hostetler, C. M.; Carter, C. S.; Solomon, M. Oxytocin and Vasopressin in Children and Adolescents with Autism Spectrum Disorders: Sex Differences and Associations with Symptoms. *Autism Res.* **2013**, *6* (2), 91–102.

https://doi.org/10.1002/aur.1270.
(14) Winslow, J. T.; Insel, T. R. Effects of Central Vasopressin Administration to Infant Rats. *Eur. J. Pharmacol* **1993**, No. 233, 101–107.
(15) Donaldson, Z. R.; Young, L. J. Oxytocin, Vasopressin, and the Neurogenetics of Sociality. *Science (80-.).* **2008**, *322* (5903), 900 LP – 904. https://doi.org/10.1126/science.1158668.
(16) Watson, S. J.; Akil, H.; Fischli, W.; Goldstein, A.; Zimmerman, E.; Nilaver, G.; van wimersma Griedanus, T. B. Dynorphin and Vasopressin: Common Localization in Magnocellular Neurons. *Science (80-.).* **1982**, *216* (4541), 85 LP – 87. https://doi.org/10.1126/science.6121376.
(17) Day, R.; Lazure, C.; Basak, A.; Boudreault, A.; Limperis, P.; Dong, W.; Lindberg, I. Prodynorphin Processing by Proprotein Convertase 2. *J. Biol. Chem.* **1998**, *273* (2), 829–836. https://doi.org/10.1074/jbc.273.2.829.
(18) Goldstein, A.; Ghazarossian, V. E. Immunoreactive Dynorphin in Pituitary and Brain. *Proc. Natl. Acad. Sci.* **1980**, *77* (10), 6207–6210. https://doi.org/10.1073/pnas.77.10.6207.
(19) Roberto, M.; Gilpin, N. W. Chapter 11 - Central Amygdala Neuroplasticity in Alcohol Dependence; Noronha, A. B. C., Cui, C., Harris, R. A., Crabbe, J. C. B. T.-N. of A. D., Eds.; Academic Press: San Diego, 2014; pp 207–226. https://doi.org/https://doi.org/10.1016/B978-0-12-405941-2.00011-0.
(20) Takahashi, A. Subchapter 7B - Dynorphin/α-Neo-Endorphin; Takei, Y., Ando, H., Tsutsui, K. B. T.-H. of H., Eds.; Academic Press: San Diego, 2016; pp 52–58. https://doi.org/https://doi.org/10.1016/B978-0-12-801028-0.00118-5.
(21) Smith, M. J.; Wise, P. M. Localization of κ Opioid Receptors in Oxytocin Magnocellular Neurons in the Paraventricular and Supraoptic Nuclei. *Brain Res.* **2001**, *898* (1), 162–165. https://doi.org/10.1016/S0006-8993(01)02154-0.
(22) Bruchas, M. R.; Land, B. B.; Chavkin, C. The Dynorphin/Kappa Opioid System as a Modulator of Stress-Induced and pro-Addictive Behaviors. *Brain Res.* **2010**, *1314*, 44–55. https://doi.org/10.1016/j.brainres.2009.08.062.
(23) Heinrichs, M.; von Dawans, B.; Domes, G. Oxytocin, Vasopressin, and Human Social Behavior. *Front. Neuroendocrinol.* **2009**, *30* (4), 548–557. https://doi.org/https://doi.org/10.1016/j.yfrne.2009.05.005.
(24) Cho, S.; Wood, A.; Bowlby, M. R. Brain Slices as Models for Neurodegenerative Disease and Screening Platforms to Identify Novel Therapeutics. *Curr. Neuropharmacol.* **2007**, *5* (1), 19–33.
(25) Huang, Y.; Williams, J. C.; Johnson, S. M. Brain Slice on a Chip: Opportunities and Challenges of Applying Microfluidic Technology to Intact Tissues. *Lab Chip* **2012**, *12* (12), 2103–2117. https://doi.org/10.1039/c2lc21142d.
(26) Rambani, K.; Vukasinovic, J.; Glezer, A.; Potter, S. M. Culturing Thick Brain Slices: An Interstitial 3D Microperfusion System for Enhanced

Viability. *J. Neurosci. Methods* **2009**, *180* (2), 243–254. https://doi.org/10.1016/J.JNEUMETH.2009.03.016.
(27) Hill, M. R. H.; Greenfield, S. A. The Membrane Chamber: A New Type of in Vitro Recording Chamber. *J. Neurosci. Methods* **2011**, *195* (1), 15–23. https://doi.org/10.1016/J.JNEUMETH.2010.10.024.
(28) See, H. H.; Ali, N. A. Electrophoresis: Principles of Capillary Electrophoresis. In *Reference Module in Chemistry, Molecular Sciences and Chemical Engineering*; Elsevier, 2018. https://doi.org/10.1016/B978-0-12-409547-2.14500-7.
(29) Paillot, R. M. SMOLUCHOWSKI. — Contribution à La Théorie de l'endosmose Électrique et de Quelques Phénomènes Corrélatifs (Bulletin de l'Académie Des Sciences de Cracovie; Mars 1903). *J. Phys. Théorique Appliquée* **1904**, *3* (1), 912–912. https://doi.org/10.1051/jphystap:019040030091201.
(30) CHAPTER 2 - THE FUNDAMENTAL NOTIONS. In *The Mathematical Foundations of the Finite Element Method with Applications to Partial Differential Equations*; Aziz, A. K. B. T.-T. M. F. of the F. E. M. with A. to P. D. E., Ed.; Academic Press, 1972; pp 15–45. https://doi.org/https://doi.org/10.1016/B978-0-12-068650-6.50008-3.
(31) Schönheinz, H. G. Strang and G. J. Fix, An Analysis of the Finite Element Method. *ZAMM - Zeitschrift für Angew. Math. und Mech.* **1975**, *55* (11), 696–697. https://doi.org/10.1002/zamm.19750551121.
(32) Garstecki, P.; Fuerstman, M. J.; Stone, H. A.; Whitesides, G. M. Formation of Droplets and Bubbles in a Microfluidic T-Junction—Scaling and Mechanism of Break-Up. *Lab Chip* **2006**, *6* (3), 437. https://doi.org/10.1039/b510841a.
(33) de Almeida Monteiro Melo Ferraz, M.; Nagashima, J. B.; Venzac, B.; Le Gac, S.; Songsasen, N. 3D Printed Mold Leachates in PDMS Microfluidic Devices. *Sci. Rep.* **2020**, *10* (1), 994. https://doi.org/10.1038/s41598-020-57816-y.
(34) Monton, M. R. N.; Terabe, S. Sample Enrichment Techniques in Capillary Electrophoresis: Focus on Peptides and Proteins. *Journal of Chromatography B: Analytical Technologies in the Biomedical and Life Sciences*. Elsevier September 1, 2006, pp 88–95. https://doi.org/10.1016/j.jchromb.2006.04.017.
(35) Giordano, B. C.; Burgi, D. S.; Hart, S. J.; Terray, A. On-Line Sample Pre-Concentration in Microfluidic Devices: A Review. *Anal. Chim. Acta* **2012**, *718*, 11–24. https://doi.org/10.1016/J.ACA.2011.12.050.
(36) Schrell, A. M.; Mukhitov, N.; Yi, L.; Adablah, J. E.; Menezes, J.; Roper, M. G. Online Fluorescence Anisotropy Immunoassay for Monitoring Insulin Secretion from Islets of Langerhans. *Anal. Methods* **2017**, *9* (1), 38–45. https://doi.org/10.1039/C6AY02899C.

APPENDIX

Chemical structures of key molecules involved in this work

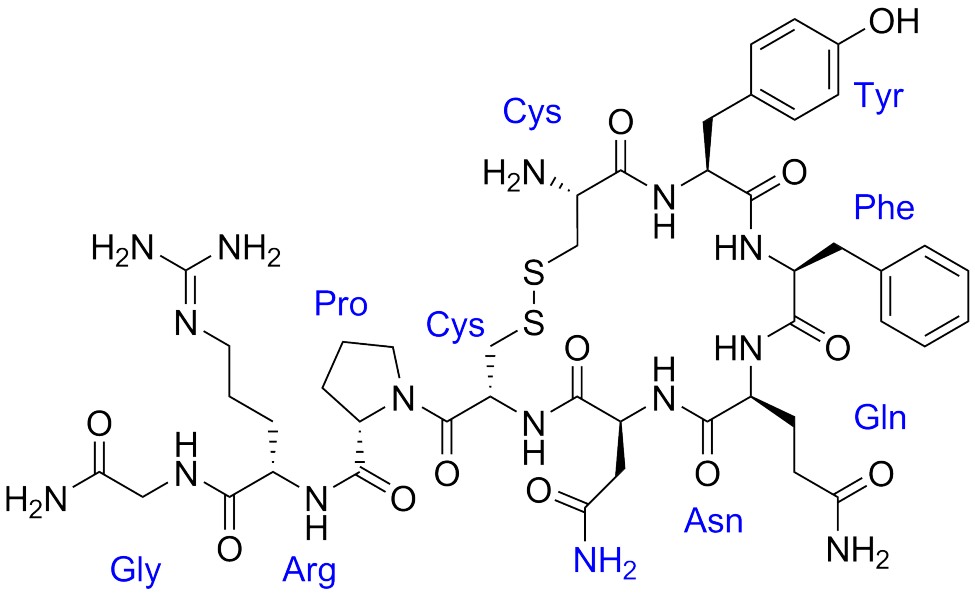

Figure A-1. *Arginine Vasopressin.* Chemical structure of Arginine vasopressin with labeled amino acids

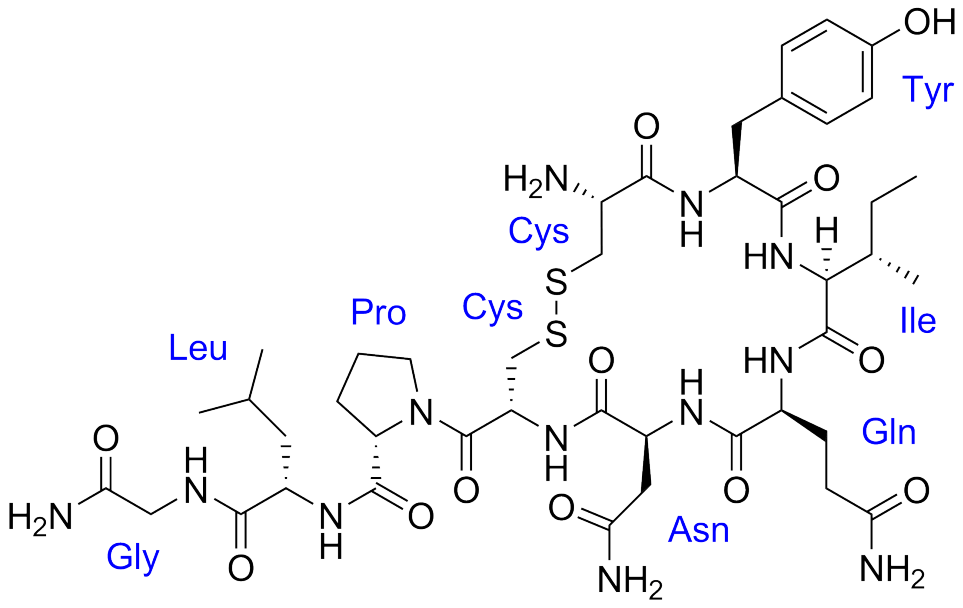

Figure A-2. *Oxytocin.* Chemical structure of Oxytocin with labeled amino acids

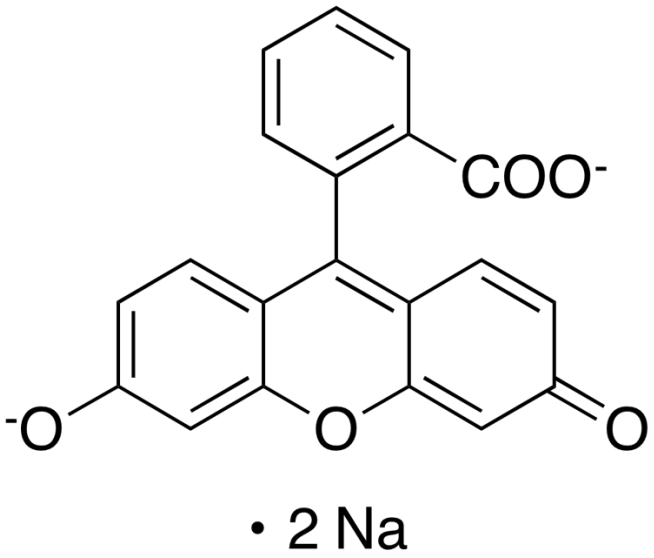

Figure A-3. *Fluorescein.* Chemical structure of fluorescein disodium salt.

VITA

Victoria Nickole Norman grew up in the small military town of Jacksonville, North Carolina before her family later moved to Upper Marlboro, Maryland, where she attended high school. Victoria later moved back to North Carolina to attend North Carolina A&T State University. She graduated with a B.S. in chemistry in May of 2018 and went on to attend graduate school at the University of Tennessee, Knoxville. Victoria enjoys reading fiction novels and trying new recipes in her free time. She will earn her M.S. in analytical chemistry in summer 2020.